Article



# Flexible and Stable N-Isopropylacrylamide/Sodium Alginate Gel Electrolytes for Aqueous Zn-$MnO_2$ Batteries

Kehuang Wang , Mingliang Shangguan , Yibo Zhao , Haoran Tian , Fu Wang , Jinliang Yuan , Lan Xia *

Posted Date: 12 June 2023

doi: 10.20944/preprints202306.0798.v1

Keywords: Zn ion battery; aqueous; hydrogel gel electrolyte; sodium alginate; N-isopropylacrylamide

*Article*

# Flexible and Stable N-Isopropylacrylamide/Sodium Alginate Gel Electrolytes for Aqueous Zn-$MnO_2$ Batteries

**Kehuang Wang, Mingliang Shangguan, Yibo Zhao, Haoran Tian, Fu Wang, Jinliang Yuan and Lan Xia ***

Faculty of Maritime and Transportation, Ningbo University, Ningbo 315211, China

**Abstract: Rechargeable** aqueous Zn-ion batteries (ZIBs) have attracted considerable attention owing to their high theoretical capacity of 820 mA h $g^{-1}$, low cost and intrinsic safety. However, the electrolyte leakage and the instability issues of Zn negative electrodes originating from side reactions between the aqueous electrolyte and Zn negative electrode, not only restricts the battery stability but also results in short-circuit of aqueous ZIBs. Herein we report a flexible and stable N-isopropylacrylamide/sodium alginate (N-SA) gel electrolyte, which possesses high mechanical strength and high ionic conductivity of $2.96\times10^{-2}$ S $cm^{-1}$, and enables the Zn metal negative electrode and $MnO_2$ positive electrode to reversibly and stably cycle. Compared to the liquid electrolyte, the N-SA hydrogel electrolyte can effectively form a uniform Zn deposition and suppress the generation of irreversible by-products. The assemble symmetric Zn/Zn cells at a current density of 1 mA $cm^{-2}$ shows a stable voltage profile, which maintains a low level of about 100 mV over 2600 h without an obvious short circuit or any overpotential increasing. Specially, the assembled Zn/N-SA/$MnO_2$ batteries can deliver a high specific capacity of 182 mAh $g^{-1}$ and maintain 98% capacity retention after 650 cycles at 0.5 A $g^{-1}$. This work provides a facile method to fabricate high-performance SA-based hydrogel electrolytes that illustrates their potential for flexible batteries for wearable electronics.

**Keywords:** Zn ion battery; aqueous; hydrogel gel electrolyte; sodium alginate; N-isopropylacrylamide

## 1. Introduction

With the development of wearable devices and electric vehicles, there is a high demand for sustainable energy storage systems. Lithium-ion batteries (LIBs) are currently being extensively studied for high energy-density, wide electrochemical window and long cycle life [1]. However, because of the limited resources of lithium, the high cost and the toxicity and flammability of organic electrolytes, LIBs assembled with organic electrolytes result in environmental pollution and poor safety performance. Also, the use of organic liquid electrolytes have the inevitable leakage, poor flexibility, etc. [2]. Compared to organic electrolyte systems, aqueous rechargeable batteries are expected to be used on a large scale in the energy storage field due to their low production cost, environmental friendliness and high safety performance. In recent years, various aqueous batteries with multivalent metal ions ($Zn^{2+}$, $Mg^{2+}$, $Ca^{2+}$ and $Al^{3+}$) have been widely reported [3]. Among them, the reserves of metallic Zn is 300 times than that of Li in the lithosphere. Aqueous zinc ion batteries (ZIBs) possess high theoretical specific capacity (820 mAh $g^{-1}$ or 5854 mAh $cm^{-3}$ )[4], low toxicity, low fabrication cost, low redox potential (–0.76 V) [5], and inherent safety. However, current aqueous zinc ion batteries have a series of problems during long cyclic life, such as the corrosion of Zn negative electrode [6] and the formation of Zn dendrites [7]. Even, Zn dendrites might cause the separator to be punctured [8] and then easily induce short circuit inside batteries [9]. There are extensive research efforts on improving theirs cycling stabilities, for example, through interfacial modification of the zinc negative electrode, electrolyte formulation optimization and hydrogel electrolytes [10]. Hydrogels are composed of polymers with hydrophilic functional groups, which promote water storage and structural integrity through weak physical hydrogen bonding. Meanwhile, polymer gel

 doi:10.20944/preprints202306.0798.v1



electrolytes act both as an electrolyte and as a separator, which can effectively avoid electrolyte leaking. Besides, hydrogel gel electrolytes ensures close contact between electrode and electrolyte, maintaining the integrity of the flexible ZIBs under external strain [11].

Presently, some hydrogel gel electrolytes reported so far are based on synthetic polymers, such as polyacrylamide (PAM) [12], polyvinyl alcohol (PVA) [13], and polyacrylic acid (PAA) [14], etc. Unfortunately, these hydrogels' either poor mechanical strength or low ionic conductivity remains challenging. On the other hand, polymer hydrogels derived from nature matrices, such as sodium alginate (SA) [15], guar gum (GG) [16], xanthan gum (XG) [17] and gelatin [18], are cheap, biocompatible and hydrophilic, and widely used in flexible Zn-ion batteries. They are multiply cross-linked internally by hydrogen, ionic and covalent bonds to obtain a stable three-dimensional network structure, which results in improving their mechanical properties and ionic conductivities. A classical development in ZIBs hydrogel gel electrolytes is the use of sodium alginate (SA) as a polymer matrix to form a hierarchically three-dimensional $Zn^{2+}$-conductor gel electrolyte. SA consists of two monomer units, $\beta$-D-mannuronic acid (M-block) and $\alpha$-L-guluronic acid (G-block) [19]. Because of SA possessing high concentration of polar groups, high modulus and easy cross-linking with $Zn^{2+}$, many strategies based on natural polysaccharide-SA, such as guar gum/SA/glycol [20], SA-polyacrylamide [21] and gelatin/SA [22], has been proposed to construct high performance ZIBs hydrogel gel electrolytes. These SA-based hydrogels exhibit high mechanical strength but they suffer from toxic raw materials [23], invoking inert crosslinker initiators [24] and complex preparation process [25].

Hence, in this work, we prepare a flexible and stable N-isopropylacrylamide (NIPAM)/sodium alginate ZIBs hydrogel gel electrolytes (noted as N-SA) via a simple chain entanglement method. We directly incorporate NIPAM into the SA hydrogel to further enhance its mechanical strength and ionic conductivity. By soaking in 4 mol $L^{-1}$ (M) $ZnSO_4$ and 0.1 M $MnSO_4$ aqueous solution, the chain entanglements of short-chain NIPAM were formed. During soaking process, $Zn^{2+}$, $Mn^{2+}$ and $SO_4^{2-}$ ions could penetrate into the N-SA hydrogel matrix and give the high conductivity of the N-SA hydrogels. Thus, due to NIPAM chain entanglements, the N-SA hydrogels show a high conductivity of $2.96\times10^{-2}$ S $cm^{-1}$ at room temperature, and this hydrogel can effectively form a uniform Zn deposition and suppress side reaction. Specially, the assembled Zn/N-SA/$MnO_2$ batteries can deliver the highest capacity of 182 mAh $g^{-1}$ (~98% retention) at a current density of 0.5 A $g^{-1}$ after 650 cycles. Therefore, this work provides a facile method to fabricate high-performance SA-based hydrogel electrolytes that illustrates their potential for flexible batteries for wearable electronics.

## 2. Experimental methods

### *2.1. Materials*

Sodium alginate (SA, M=398.31 g $mol^{-1}$, AR, >99%) and $ZnSO_4\bullet7H_2O$ (ACS, 99%) were purchased from Aladdin Chemical Reagent Co., Ltd. $MnSO_4\bullet H_2O$ (AR, 99%), N-isopropylacrylamide (NIPAM, AR, >99%) and ammonium chloride ($NH_4Cl$, AR, 99%) were purchased from Macklin Chemical Reagent Co., Ltd. Potassium permanganate ($KMnO_4$, AR, 99%) was also purchased from Macklin Chemical Reagent Co., Ltd. All chemicals were directly used with no purification treatment.

### *2.2. Preparation of $\alpha$-$MnO_2$ powders*

The $\alpha$-$MnO_2$ powder was prepared according to the literature method [26]. The general experimental process is as follows: $KMnO_4$ and $NH_4Cl$ were subsequently completely dissolved in deionized water and then mixed homogeneously. Then, the solution was placed in a Teflon-lined reactor under hydrothermal conditions at 140°C for 24 hours. The obtained powder was filtered, washed with plenty of water, and dried.

### *2.3. Preparation of electrolytes*

The sodium alginate (SA) and NIPAM-SA (N-SA) hydrogel electrolyte was prepared by a uniform casting method and subsequently soaked in 4 mol $L^{-1}$ (M) $ZnSO_4$ and 0.1 M $MnSO_4$ aqueous

 doi:10.20944/preprints202306.0798.v1



solution. Briefly, 1.2 g SA (or 1.2 g SA and 0.15g NIPAM) were dissolved into 30 mL deionized water and stirred at 60℃ for 0.5h. The as-prepared homogeneous composite solution was then poured into a glass pane and then immersed in 4 mol $ZnSO_4$ and 0.1 $MnSO_4$ for 0.5h. The resulting composite gel is noted as SA and N-SA, respectively.

*2.4. Preparation of electrode and battery assembly*

$MnO_2$ electrodes include 70 wt.% of $\alpha$-$MnO_2$ powders, 20 wt.% of Super P (SP), and 10 wt.% of carboxymethyl cellulose (CMC). The current collect is the Ti foil. The active mass loading of the $MnO_2$ electrodes is ~1.5 mg $cm^{-2}$. All 2032 coin-cells are directly assembled in air.

*2.5. Characterizations*

A Fourier transform infrared spectrometer (FTIR, Nicolet 6700) was used to characterize the samples. The micrometer was used for measuring the thickness of the N-SA hydrogel electrolyte. A field-emission scanning electron microscope (SEM, Sirion200, FEI) was employed to determine the morphology of gel electrolytes and electrodes. X-ray diffraction (XRD, D8 DISCOVER, Bruker, Germany) was used to character the surface of Zn negative electrodes.

Linear scanning voltammetry (LSV), electrochemical impedance spectroscopy (EIS), corrosion tests, and cyclic voltammetry (CV) were carried out on an electrochemical workstation (CHI 660E, Shanghai Chenhua Instrument Co., Ltd., Shanghai, China). The EIS measurements were tested in the frequency range of 10 mHz to 10 kHz with the oscillation amplitude of 5 mV. Galvanostatic charge-discharge (GCD) and rate performance measurements were performed on a CT3001A Land battery testing system (Wuhan Land Electronic Co., Ltd, Wuhan, China). EIS measurements were used to calculate the ionic conductivity ($\sigma$) of the electrolytes through stainless steel (SS)||electrolyte||SS symmetrical coin-cells according to the reported reference method [27]. LSV curves were measured using a SS||electrolyte||Zn coin-cells at a scan rate of 1 mV $s^{-1}$ to investigate the electrochemical window of the electrolytes. CV curves of Zn||electrolyte||$MnO_2$ asymmetrical coin-cells were obtained at a scan rate of 1 mV $s^{-1}$.

**3. Results and Discussion**

The preparation process of the N-SA gel electrolyte is shown in Figure 1a. The N-SA aqueous solution is a transparent and homogeneous viscous liquid with disordered molecular chains. After adding 4 M $ZnSO_4$ + 0.1 M $MnSO_4$ solution into N-SA aqueous liquid solution for 30 min, the N-SA gel electrolyte with cross-linked structures is online formed through $Zn^{2+}$ coordinating function [20]. Figure 1b-c shows an optical image of a uniform N-SA electrolyte, which is transparent and has excellent flexibility. The N-SA gel electrolyte can be bent at any angles and has a thickness of 325 μm as shown in Figure 1d. The FTIR spectra of the SA and N-SA hydrogel electrolyte as well as pure SA and NIPAM powder were collected as shown in Figure 1e. For the pure SA, the absorption peaks at 1590 $cm^{-1}$ and 1401 $cm^{-1}$ are attributed to the asymmetric stretching vibrations and symmetric stretching vibrations of $-COO^-$ groups on the SA chains, respectively. In contrast, for the SA and N-SA hydrogel electrolyte, these two peaks shift to higher values because of coordinate bonds between $-COO^-$ groups and $Zn^{2+}$ [28]. Peaks were observed in the spectra of NIPAM at 532 $cm^{-1}$ and 1517 $cm^{-1}$, which assigned to the -NH wagging vibration and the C=O stretching vibration, respectively [29]. For the N-SA hydrogel, these similar characteristic peaks also appear, which suggests the presence of NIPAM. The surface morphology of the N-SA gel electrolyte has uniformity and even (Figure 1f). As determined by the cross-sectional morphology (Figure 1d), the thickness of the N-SA gel electrolyte is 60 $\mu$m, which is lower than the thickness measured by micrometer. This reason is that the sample of SEM images is dried through freezing treatment.

 doi:10.20944/preprints202306.0798.v1



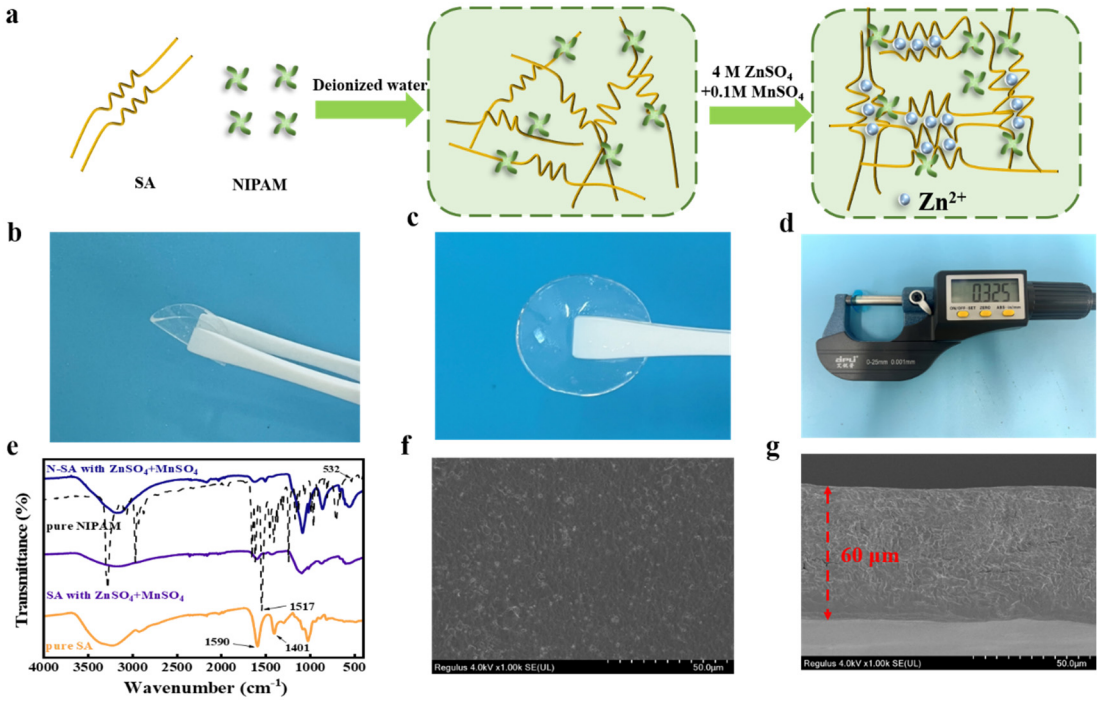


**Figure 1.** (a) Schematic diagram of the preparation of the N-SA hydrogel electrolyte. (b-c) Photographs of the N-SA hydrogel electrolyte. (d) Thickness measurement diagram of the N-SA hydrogel electrolyte. (e) FTIR spectra of pure SA, pure NIPAM, SA and N-SA with $ZnSO_4$+$MnSO_4$. The SEM image of surface (f) and cross-sectional (g) morphology of the N-SA hydrogel electrolyte.

Figure 2a shows EIS spectra of stainless steel (SS)/SS symmetrical batteries with the liquid, SA and N-SA gel electrolyte at room temperature. The corresponding ionic conductivity was calculated by the reported method [30]. Notably, the N-SA gel electrolyte shows a high ionic conductivity of $2.96\times10^{-2}$ S $cm^{-1}$, which is higher than that of the SA gel electrolyte and liquid electrolyte. LSV tests were conducted to evaluate the electrochemical stability of the electrolyte. As shown in Figure 2b, the oxidation potential of the N-SA gel electrolyte is 2.51V (vs. $Zn^{2+}$/Zn). The LSV curve of the cells with the N-SA gel electrolyte also exhibits a reduction potential of (–0.15 V vs. $Zn^{2+}$/Zn), which is lower than that of cells with liquid electrolyte (–0.094 V vs. $Zn^{2+}$/Zn). These LSV results suggest that the N-SA gel electrolyte has a wide electrochemical window. In addition, we tested the CV curves of Zn/Zn symmetric cells at 1 mV $s^{-1}$ as shown in Figure S1. The nucleation overpotential of $Zn^{2+}$ in the N-SA hydrogel electrolyte is greater than that in the liquid electrolyte. The larger nucleation overpotential indicates a smaller nucleation radius, implying an easier homogeneous deposition. This demonstrates that the N-SA gel electrolyte is beneficial for small, denser and homogeneous of Zn deposition [31]. Furthermore, the Tafel curve was used to measure the corrosion of Zn foil in the electrolyte as shown in Figure 2c. Compared to the liquid electrolyte, the corrosion potential of zinc with the N-SA gel electrolyte is increased from –0.0084 to 0.0177 V, and corrosion current of zinc with the N-SA gel electrolyte is decreased from –5.984 to –5.286 A. Higher corrosion potentials and lower corrosion currents indicate a smaller tendency for corrosion reactions and lower corrosion rates, respectively[32].

The Zn/Cu asymmetric cells with different electrolytes were used to study the cycling stability of zinc plating/stripping in this work. As shown in Figure 2d-f, we compare the voltage/capacity curves of Zn/Cu of the N-SA, SA hydrogel electrolyte and liquid electrolyte for different numbers of cycles. For the N-SA cells cycled at 1 mA $cm^{-2}$, the discharge/charge behavior kept the same over 500 cycles (see Figure S2). However, the voltage profile of cells with the liquid electrolyte is increased during both the discharge and charge process. This means that the polarization potential of the N-SA hydrogel electrolyte was considerably lower than those of the liquid electrolyte and SA hydrogel electrolyte. The low polarization potential of zinc plating/stripping in the N-SA hydrogel electrolyte

 doi:10.20944/preprints202306.0798.v1



is beneficial for the uniformity of zinc deposition [33]. Notably, the coulomb efficiency (CE) is a crucial parameter for investigating the reversibility and stability of the zinc negative electrode [34]. As shown in Figure 2e, the coulombic efficiency of the N-SA hydrogel cell increases from 86% in the first cycle to 98% after 20 cycles and remains stable at 99% for subsequent cycles. Meanwhile, the Zn/Cu cell with the N-SA hydrogel electrolyte can be stably cycled at 1 mA $cm^{-2}$ for more than 500 cycles. In contrast, the CE of Zn/Cu cells with the liquid electrolyte and SA hydrogel electrolyte quickly decreases to 0 after 83 and 200 cycles, respectively. The high and stable coulombic efficiency of the N-SA cell is probably because the side reactions and dendrite growth are significantly restrained. Figure 2h-i shows SEM images of Cu foils after Zn deposition for 5 h at 2 mA $cm^{-2}$ in the Zn/Cu asymmetric cells with the N-SA hydrogel electrolyte and liquid electrolyte. For the liquid electrolyte, a large numbers of micron-grade dead Zn particles with irregular shapes appear on the surface of Cu, which is adverse for a high plating/stripping efficiency. By contrast, the deposited Zn is uniform and smoothly in the N-SA hydrogel electrolyte as shown in Figure 2h. Therefore, this N-SA hydrogel electrolyte indicates a homogeneous nucleation process of zinc deposition.

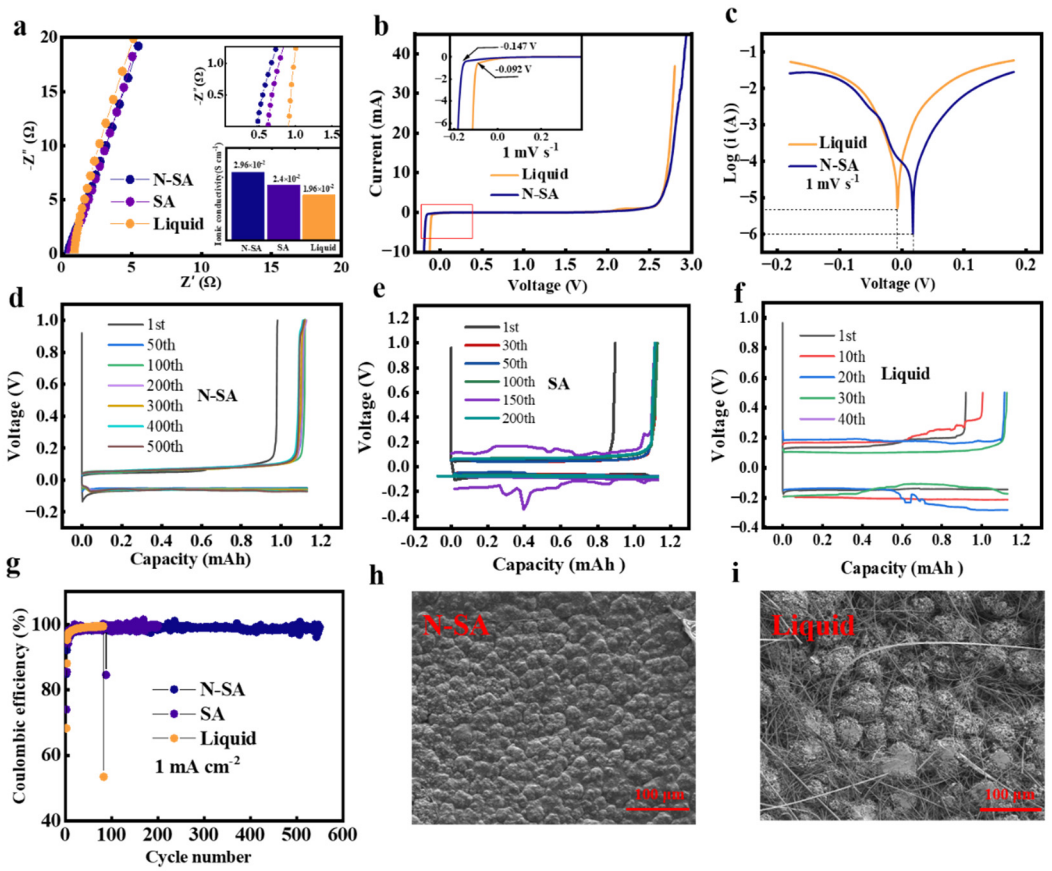


**Figure 2.** (a) EIS spectra of stainless steel (SS)/SS symmetrical batteries with the liquid, SA and N-SA gel electrolyte. (b) LSV profiles of the liquid and N-SA gel electrolyte using stainless steel (SS)/Zn coin-cells at 1 mV $s^{-1}$. (c) Linear polarization curves generated for the liquid and N-SA gel electrolyte using Zn/Zn coin-cells at 1 mV $s^{-1}$. Voltage/capacity curves of Zn/Cu cells with the N-SA electrolyte (d), SA gel electrolyte (e) and liquid electrolyte (f) at 1 mA $cm^{-2}$. (g) The coulombic efficiency of the Zn/Cu asymmetric cells with the liquid, N-SA and SA gel electrolyte. SEM images of Cu foils after Zn deposition for 5 h at 2 mA $cm^{-2}$ in the Zn/Cu asymmetric cells with the N-SA hydrogel electrolyte (h) and liquid electrolyte (i).

Long-term cycling property of the symmetric Zn/Zn cells with the N-SA hydrogel electrolyte and liquid electrolyte at a current density of 1 mA $cm^{-2}$ is shown in Figure 3a-c. The cell with N-SA hydrogel electrolyte shows a stable voltage profile, which maintains a low level of about 100 mV over 2600 h without an obvious short circuit or any overpotential increasing. In contrast, the cell with the

 doi:10.20944/preprints202306.0798.v1



liquid electrolyte exhibits a sudden increase in polarization during the cycling process. This indicates that the N-SA hydrogel electrolyte possesses a stable Zn stripping/plating process. Furthermore, the voltage profiles of the Zn/Zn symmetrical cell with the N-SA gel electrolyte and liquid electrolyte were investigated for different current densities from 0.1 to 2.0 mA $cm^{-2}$, as shown in Figure 3d. When the current density increased from 0.1 mA $cm^{-2}$ to 2.0 mA $cm^{-2}$, the polarization voltages of the N-SA cells are always below 200 mV. However, the symmetric Zn cell with the liquid electrolyte suffer from shorts circuit. This suggests that the N-SA gel electrolyte is a promising candidate for ZIBs at wide current densities. The XRD patterns of the Zn negative electrode collected from the N-SA cells after 30 cycles displays similar signals compared to that of fresh Zn foils (Figure 3e). However, the XRD patterns of Zn negative electrode cycled in the liquid electrolyte appear several new obvious peaks located at 8.2º, 16.3º and 24.5º (2θ). These peaks suggest the formation of $Zn_4SO_4(OH)_6 \cdot 5H_2O$ (PDF#69-0688). This indicates that the N-SA hydrogel significantly inhibits interfacial side reactions, reduces the production of "dead" zinc, and results in a highly reversible and efficient plating/stripping of zinc ions.

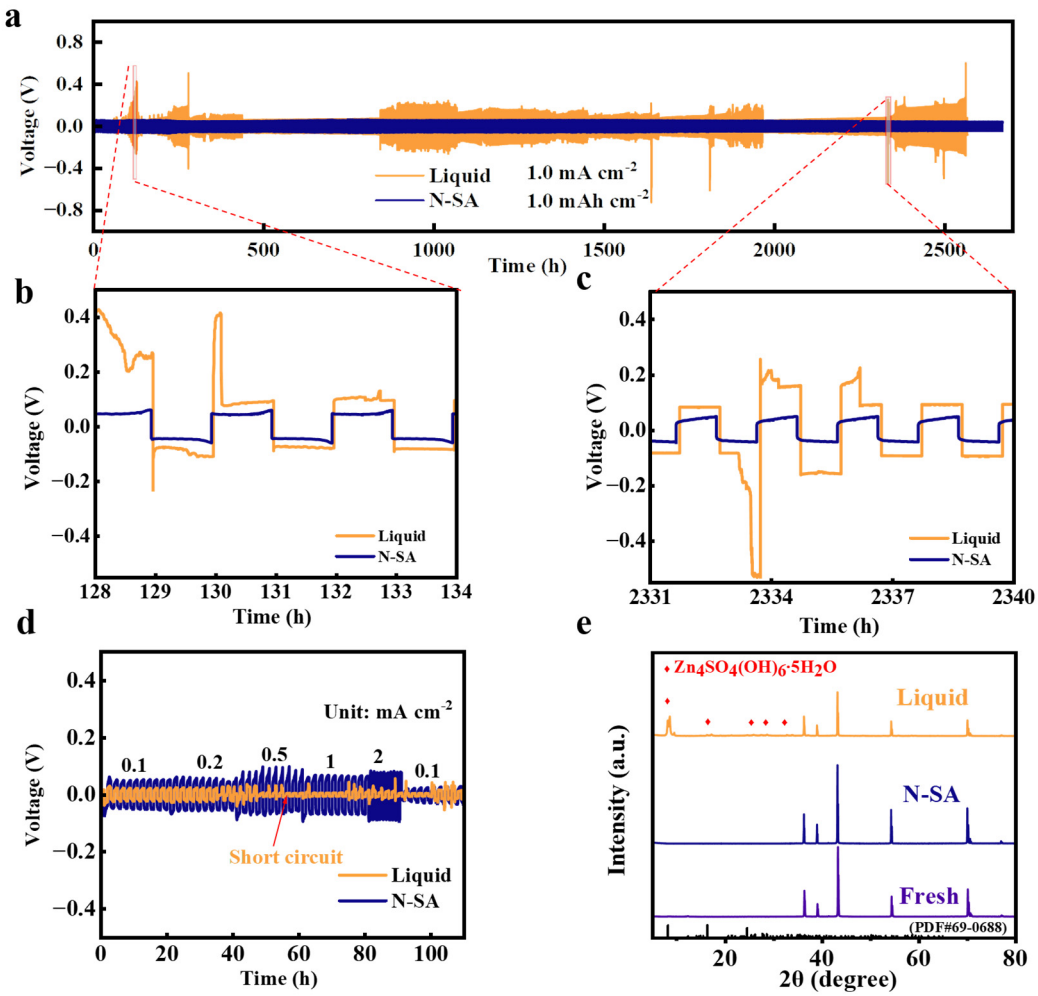


**Figure 3.** (a-c) Galvanostatic Zn plating/stripping of Zn/Zn symmetrical cells of the N-SA gel electrolyte and liquid electrolyte at a current density of 1 mA $cm^{-2}$ (capacity: 1 mAh $cm^{-2}$). (d) Voltage profiles of the Zn/Zn symmetrical cell with the N-SA gel electrolyte and liquid electrolyte for different current densities. (e) XRD patterns of the Zn negative electrode of the symmetrical cell after 30 cycles at 1 mA $cm^{-2}$.

Electrochemical performance of Zn/$MnO_2$ cells with the N-SA, SA hydrogel electrolyte and liquid electrolyte at 25°C was shown in Figure 4. Figure 4a shows CV curves of the cells with the N-SA hydrogel electrolyte at 0.1 mV $s^{-1}$ in the voltage range of 0.9~1.9 V at room temperature. The first

 doi:10.20944/preprints202306.0798.v1



cycle shows a single reduction peak at approximately ~1.17 V, while two reduction peaks at ~1.34 and ~1.22 V appear in the following cycles. The change in the peak number and position is attributed to the phase transition and morphology evolution during the first cycle [35]. In the oxidation reaction, two overlapped peaks at 1.59 and 1.62 V are observed. This indicates a $Zn^{2+}$ insertion and extraction process in the charge storage mechanism [35]. Besides, the CV curves in the second and third cycles nearly overlap, suggesting the electrochemical reversibility of the cells. As displayed in Figure 4b-c, the Zn/$MnO_2$ cells with the N-SA hydrogel electrolyte exhibit reversible capacities of 310, 266, 176, and 104 mAh $g^{-1}$ at current densities of 0.1, 0.2, 0.5, and 1 A $g^{-1}$, respectively. When the current density decreases back to 0.5 mA $cm^{-2}$, the capacities immediately recover to 180 mAh $g^{-1}$. Thus, the cell with the N-SA hydrogel electrolyte exhibits a good rate performance. Long-term cycling stabilities of the Zn/$MnO_2$ cells with the N-SA, SA hydrogel electrolyte and liquid electrolyte at 0.5 A $g^{-1}$ are shown in Figure 4d. The Zn/$MnO_2$ cells with the N-SA hydrogel electrolyte maintain superior cycling stability compared to the cells in the SA and liquid electrolyte. The reversible capacities are 169, 171, 188, 185, and 182 mAh $g^{-1}$ after 10, 200, 400, 500, 600 cycles (Figure S2), respectively. Even, the N-SA cell delivers a highly reversible capacity of 182 mAh $g^{-1}$ after 650 cycles, indicating a superior capacity retention of 98% and near 100% coulombic efficiency. This indicates that the N-SA hydrogel electrolyte possesses ultra-stable and highly reversible electrochemical performance during the long cycling, which maybe ascribed to the uniform Zn reversible deposition.

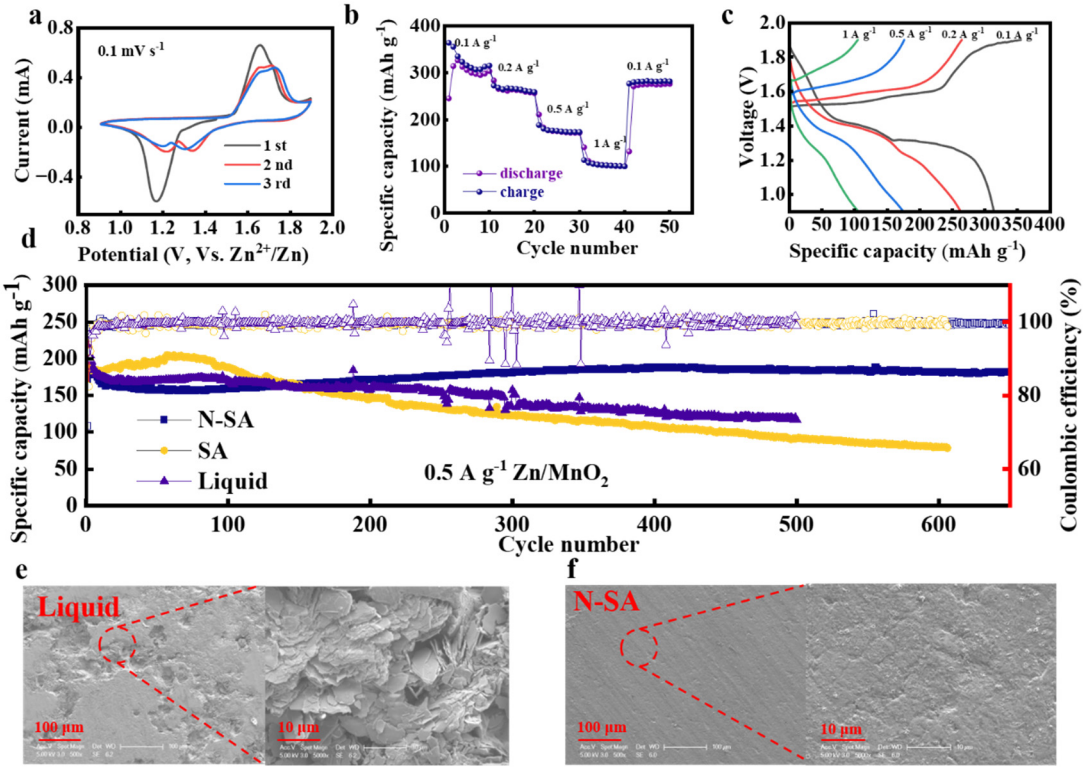


**Figure 4.** Electrochemical performance of Zn/$MnO_2$ cells with the N-SA, SA hydrogel electrolyte and liquid electrolyte at 25°C. (a) CV curves of the cells with the N-SA hydrogel electrolyte at 0.1 mV $s^{-1}$ at room temperature. (b) Rate performance of the cells with the N-SA hydrogel electrolyte. (c) Galvanostatic charge/discharge profiles at different current densities. (d) Long-term cycling stability of the Zn/$MnO_2$ cells at 0.5 A $g^{-1}$. The SEM images of the Zn negative electrodes collected from the cells with the liquid electrolyte (e) and N-SA hydrogel electrolyte (f) at 0.5 A $g^{-1}$ after 300 cycles.

After charged back to 1.9 V after 300 cycles, the corresponding SEM images of two electrodes collected from Zn/$MnO_2$ cells are shown in Figure S3 and Figure 4e-f. As depicted in Figure S3, some flake-like deposits are observed on the surface of the $MnO_2$ electrode in the liquid electrolyte after 300 cycles. In contrast to this flake-like surface, the $MnO_2$ surface collected from the N-SA hydrogel electrolytes remains relatively clean without any obvious flaked after cycling. Furthermore, as shown

 doi:10.20944/preprints202306.0798.v1



in Figure 4e-f, the SEM images of Zn electrodes are collected from Zn/$MnO_2$ cells with the N-SA hydrogel electrolyte and liquid electrolyte after 300 cycles. The corresponding SEM images of Zn electrodes cycled after 500 cycles are also displayed in Figure S4. It can be found that after cycling in the liquid electrolyte, the uneven Zn surface with a large number of sheet-like dendrites and byproducts was observed, which may be due to the interfacial degradation of Zn with liquid electrolyte. Conversely, after cycling with the S-NA hydrogel electrolyte, the surface of Zn electrode keeps very flat and uniform. Therefore, for the N-SA hydrogel electrolyte, the parasitic reaction between electrodes and electrolyte are effectively suppressed, which results in satisfactory long-term cycling stabilities of the assembled Zn/$MnO_2$ cells.

## 4. Conclusions

In summary, the flexible and stable N-isopropylacrylamide (NIPAM)/sodium alginate ZIBs hydrogel gel electrolytes (noted as N-SA) via a simple chain entanglement method is designed. We directly incorporate NIPAM into the SA hydrogel to further enhance its mechanical strength and ionic conductivity. By soaking in 4 mol $L^{-1}$ (M) $ZnSO_4$ and 0.1 M $MnSO_4$ aqueous solution, the chain entanglements of short-chain NIPAM were formed. During soaking process, $Zn^{2+}$, $Mn^{2+}$ and $SO_4^{2-}$ ions could penetrate into the N-SA hydrogel matrix and give the high conductivity of the N-SA hydrogels. Thus, due to NIPAM chain entanglements, the N-SA hydrogels show a high conductivity of $2.96\times10^{-2}$ S $cm^{-1}$ at room temperature. Compared to the liquid electrolyte, the N-SA hydrogel electrolyte can effectively form a uniform Zn deposition and suppress the generation of irreversible by-products. The assemble symmetric Zn/Zn cells at a current density of 1 mA $cm^{-2}$ shows a stable voltage profile, which maintains a low level of about 100 mV over 2600 h without an obvious short circuit or any overpotential increasing. Specially, the assembled Zn/N-SA/$MnO_2$ batteries can deliver the highest capacity of 182 mAh $g^{-1}$ (~98% retention) at a current density of 0.5 A $g^{-1}$ after 650 cycles. Therefore, this work provides a facile method to fabricate high-performance SA-based hydrogel electrolytes that illustrates their practical applications of aqueous ZIBs.

**Supplementary Materials:** Figure S1: CV curves of symmetrical cells of the N-SA gel electrolyte and liquid electrolyte at 1 mV $s^{-1}$; Figure S2: Discharge/charge profiles of Zn/$MnO_2$ cells with the N-SA hydrogel electrolyte at different cycles; Figure S3: The SEM images of the positive electrodes collected from the cells with the liquid electrolyte (a) and N-SA hydrogel electrolyte (b) at 0.5 A $g^{-1}$ after 300 cycles; Figure S4: The SEM images of the Zn negative electrodes collected from the cells with the liquid electrolyte (a) and N-SA hydrogel electrolyte (b) at 0.5 A $g^{-1}$ after 500 cycles.

**Funding:** The authors gratefully acknowledge the support from National Natural Science Foundation of China (no. 22075155), and the Ningbo Science & Technology Innovation 2025 Major Project (no. 2021Z121).

**Conflicts of Interest:** The authors declare no conflict of interest.

## References

1. Li, M.; Lu, J.; Chen, Z.; Amine, K. 30 Years of Lithium-Ion Batteries. *Adv. Mater.* **2018**, *30*, 1800561.
2. Tang, B.; Shan, L.; Liang, S.; Zhou, J. Issues and Opportunities Facing Aqueous Zinc-Ion Batteries. *Energy Environ. Sci.* **2019**, *12*, 3288–3304.
3. Michail, A.; Silván, B.; Tapia-Ruiz, N. Progress in High-Voltage $MgMn_2O_4$ oxyspinel Cathode Materials for Mg Batteries. *Curr. Opin. Electrochem.* **2022**, *31*, 100817.
4. Fu, J.; Cano, Z.P.; Park, M.G.; Yu, A.; Fowler, M.; Chen, Z. Electrically Rechargeable Zinc-Air Batteries: Progress, Challenges, and Perspectives. *Adv. Mater.* **2017**, *29*, 1604685.
5. Mainar, A.R.; Colmenares, L.C.; Blázquez, J.A.; Urdampilleta, I. A Brief Overview of Secondary Zinc Anode Development: The Key of Improving Zinc-Based Energy Storage Systems. *Int. J. Energy Res.* **2018**.
6. Wang, R.; Yao, M.; Huang, S.; Tian, J.; Niu, Z. Sustainable Dough-Based Gel Electrolytes for Aqueous Energy Storage Devices. *Adv. Funct. Mater.* **2021**, *31*, 2009209.
7. Xue, T.; Fan, H.J. From Aqueous Zn-Ion Battery to Zn-$MnO_2$ Flow Battery: A Brief Story. *J. Energy Chem.* **2021**, *54*, 194–201.
8. Wang, F.; Borodin, O.; Gao, T.; Fan, X.; Sun, W.; Han, F.; Faraone, A.; Dura, J.A.; Xu, K.; Wang, C. Highly Reversible Zinc Metal Anode for Aqueous Batteries. *Nat. Mater.* **2018**, *17*, 543–549.
9. Pu, X.; Jiang, B.; Wang, X.; Liu, W.; Dong, L.; Kang, F.; Xu, C. High-Performance Aqueous Zinc-Ion Batteries Realized by MOF Materials. *Nano-Micro Lett.* **2020**, *12*, 152.

10. Parker, J.F.; Chervin, C.N.; Pala, I.R.; Machler, M.; Burz, M.F.; Long, J.W.; Rolison, D.R. Rechargeable Nickel–3D Zinc Batteries: An Energy-Dense, Safer Alternative to Lithium-Ion. *Science* **2017**, *356*.
11. Chen, M.; Zhou, W.; Wang, A.; Huang, A.; Chen, J.; Xu, J.; Wong, C.-P. Anti-Freezing Flexible Aqueous Zn–$MnO_2$ Batteries Working at −35 °C Enabled by a Borax-Crosslinked Polyvinyl Alcohol/Glycerol Gel Electrolyte. *J. Mater. Chem. A* **2020**, *8*, 6828–6841.
12. Mo, F.; Liang, G.; Meng, Q.; Liu, Z.; Li, H.; Fan, J.; Zhi, C. A Flexible Rechargeable Aqueous Zinc Manganese-Dioxide Battery Working at −20 °C. *Energy Environ. Sci.* **2019**, *12*, 706–715.
13. Chen, M.; Zhou, W.; Wang, A.; Huang, A.; Chen, J.; Xu, J.; Wong, C.-P. Anti-Freezing Flexible Aqueous Zn–$MnO_2$ Batteries Working at −35 °C Enabled by a Borax-Crosslinked Polyvinyl Alcohol/Glycerol Gel Electrolyte. *J. Mater. Chem. A* **2020**, *8*, 6828–6841.
14. Gaikwad, A.M.; Whiting, G.L.; Steingart, D.A.; Arias, A.C. Highly Flexible, Printed Alkaline Batteries Based on Mesh-Embedded Electrodes. *Adv. Mater.* **2011**, *23*, 3251–3255.
15. Tang, Y.; Liu, C.; Zhu, H.; Xie, X.; Gao, J.; Deng, C.; Han, M.; Liang, S.; Zhou, J. Ion-Confinement Effect Enabled by Gel Electrolyte for Highly Reversible Dendrite-Free Zinc Metal Anode. *Energy Storage Mater.* **2020**, *27*, 109–116.
16. Huang, Y.; Zhang, J.; Liu, J.; Li, Z.; Jin, S.; Li, Z.; Zhang, S.; Zhou, H. Flexible and Stable Quasi-Solid-State Zinc Ion Battery with Conductive Guar Gum Electrolyte. *Mater. Today Energy* **2019**, *14*, 100349.
17. Wang, Y.; Chen, Y. A Flexible Zinc-Ion Battery Based on the Optimized Concentrated Hydrogel Electrolyte for Enhanced Performance at Subzero Temperature. *Electrochemical Acta* **2021**, *395*, 139178.
18. Han, Q.; Chi, X.; Zhang, S.; Liu, Y.; Zhou, B.; Yang, J.; Liu, Y. Durable, Flexible Self-Standing Hydrogel Electrolytes Enabling High-Safety Rechargeable Solid-State Zinc Metal Batteries. *J. Mater. Chem. A* **2018**, *6*, 23046–23054.
19. Hu, O.; Chen, G.; Gu, J.; Lu, J.; Zhang, J.; Zhang, X.; Hou, L.; Jiang, X. A Facile Preparation Method for Anti-Freezing, Tough, Transparent, Conductive and Thermoplastic Poly (Vinyl Alcohol)/Sodium Alginate/Glycerol Organohydrogen Electrolyte. *Int. J. Biol. Macromol.* **2020**, *164*, 2512–2523.
20. Wang, J.; Huang, Y.; Liu, B.; Li, Z.; Zhang, J.; Yang, G.; Hiralal, P.; Jin, S.; Zhou, H. Flexible and Anti-Freezing Zinc-Ion Batteries Using a Guar-Gum/Sodium-Alginate/Ethylene-Glycol Hydrogel Electrolyte. *Energy Storage Mater.* **2021**, *41*, 599–605.
21. Dong, H.; Li, J.; Zhao, S.; Jiao, Y.; Chen, J.; Tan, Y.; Brett, D.J.L.; He, G.; Parkin, I.P. Investigation of a Biomass Hydrogel Electrolyte Naturally Stabilizing Cathodes for Zinc-Ion Batteries. *ACS Appl. Mater. Interfaces* **2021**, *13*, 745–754.
22. Lu, Y.; Zhu, T.; Xu, N.; Huang, K. A Semisolid Electrolyte for Flexible Zn-Ion Batteries. *ACS Appl. Energy Mater.* **2019**, *2*, 6904–6910.
23. Deng, W.; Zhou, Z.; Li, Y.; Zhang, M.; Yuan, X.; Hu, J.; Li, Z.; Li, C.; Li, R. High-Capacity Layered Magnesium Vanadate with Concentrated Gel Electrolyte toward High-Performance and Wide-Temperature Zinc-Ion Battery. *ACS Nano* **2020**, *14*, 15776–15785.
24. Shih, H.; Liu, H.-Y.; Lin, C.-C. Improving Gelation Efficiency and Cytocompatibility of Visible Light Polymerized Thiol-Norbornene Hydrogels via Addition of Soluble Tyrosine. *Biomatter. Sci.* **2017**, *5*, 589–599.
25. Song, Z.; Ding, J.; Liu, B.; Liu, X.; Han, X.; Deng, Y.; Hu, W.; Zhong, C. A Rechargeable Zn–Air Battery with High Energy Efficiency and Long Life Enabled by a Highly Water-Retentive Gel Electrolyte with Reaction Modifier. *Adv. Mater.* **2020**, *32*, 1908127.
26. Lee, B.; Lee, H.R.; Kim, H.; Chung, K.Y.; Cho, B.W.; Oh, S.H. Elucidating the Intercalation Mechanism of Zinc Ions into $\alpha$-$MnO_2$ for Rechargeable Zinc Batteries. *Chem. Commun.* **2015**, *51*, 9265–9268.
27. Liu, Z.-F.; Zhu, C.-Y.; Ye, Y.-W.; Zhang, Y.-H.; Cheng, F.; Li, H.-R. Synergistic Optimization Strategy Involving Sandwich-like $MnO_2$ @rGO and Laponite-Modified PAM for High-Performance Zinc-Ion Batteries and Zinc Dendrite Suppression. *ACS Appl. Mater. Interfaces* **2022**, *14*, 25962–25971.
28. Tang, Y.; Liu, C.; Zhu, H.; Xie, X.; Gao, J.; Deng, C.; Han, M.; Liang, S.; Zhou, J. Ion-Confinement Effect Enabled by Gel Electrolyte for Highly Reversible Dendrite-Free Zinc Metal Anode. *Energy Storage Mater.* **2020**, *27*, 109–116.
29. Zeng, X.; Meng, X.; Jiang, W.; Ling, M.; Yan, L.; Liang, C. In-Situ Constructing Polyacrylamide Interphase Enables Dendrite-Free Zinc Anode in Aqueous Batteries. *Electrochimica Acta* **2021**, *378*, 138106.
30. Hu, Y.; Shen, P.; Zeng, N.; Wang, L.; Yan, D.; Cui, L.; Yang, K.; Zhai, C. Hybrid Hydrogel Electrolyte Based on Metal–Organic Supermolecular Self-Assembly and Polymer Chemical Cross-Linking for Rechargeable Aqueous Zn–$MnO_2$ Batteries. *ACS Appl. Mater. Interfaces* **2020**, *12*, 42285–42293.
31. Wei, T.; Ren, Y.; Li, Z.; Zhang, X.; Ji, D.; Hu, L. Bonding Interaction Regulation in Hydrogel Electrolyte Enable Dendrite-Free Aqueous Zinc-Ion Batteries from −20 to 60 °C. *Chem. Eng. J.* **2022**, *434*, 134646.
32. Ma, L.; Chen, S.; Li, N.; Liu, Z.; Tang, Z.; Zapien, J.A.; Chen, S.; Fan, J.; Zhi, C. Hydrogen-Free and Dendrite-Free All-Solid-State Zn-Ion Batteries. *Adv. Mater.* **2020**, *32*, 1908121.
33. Hong, Z.; Ahmad, Z.; Viswanathan, V. Design Principles for Dendrite Suppression with Porous Polymer/Aqueous Solution Hybrid Electrolyte for Zn Metal Anodes. *ACS Energy Lett.* **2020**, *5*, 2466–2474.

 doi:10.20944/preprints202306.0798.v1



34. Kim, J.Y.; Liu, G.; Shim, G.Y.; Kim, H.; Lee, J.K. Functionalized Zn @ZnO Hexagonal Pyramid Array for Dendrite-Free and Ultrastable Zinc Metal Anodes. *Adv. Funct. Mater.* **2020**, *30*, 2004210.
35. Pan, H.; Shao, Y.; Yan, P.; Cheng, Y.; Han, K.S.; Nie, Z.; Wang, C.; Yang, J.; Li, X.; Bhattacharya, P.; et al. Reversible Aqueous Zinc/Manganese Oxide Energy Storage from Conversion Reactions. *Nat. ENERGY* **2016**, *1*.